INTERNATIONAL JOURNAL FOR NUMERICAL METHODS IN FLUIDS
Int. J. Numer. Meth. Fluids (2009)
Published online in Wiley InterScience (www.interscience.wiley.com). DOI: 10.1002/fld.2126

An evaluation of a 3D free-energy-based lattice Boltzmann model for multiphase flows with large density ratio

Haibo Huang[1,*,†], Hongwei Zheng[2], Xi-yun Lu[1] and Chang Shu[3]

[1]*Department of Modern Mechanics, University of Science and Technology of China, Hefei 230027, China*
[2]*Department of Mechanical Engineering, The University of Sheffield, U.K.*
[3]*National University of Singapore, Singapore*

SUMMARY

In this paper, the 3D Navier–Stokes (N–S) equation and Cahn–Hilliard (C–H) equations were solved using a free-energy-based lattice Boltzmann (LB) model. In this model, a LB equation with a D3Q19 velocity model is used to recover continuity and N–S equations while another LB equation with D3Q7 velocity model for solving C–H equation (*Int. J. Numer. Meth. Fluids*, 2008; **56**:1653–1671) is applied to solve the 3D C–H equation.

To avoid the excessive use of computational resources, a moving reference frame is adopted to allow long-time simulation of a bubble rising. How to handle the inlet/outlet and moving-wall boundary conditions are suggested. These boundary conditions are simple and easy for implementation.

This model's performance on two-phase flows was investigated and the mass conservation of this model was evaluated. The model is validated by its application to simulate the 3D air bubble rising in viscous liquid (density ratio is 1000). Good agreement was obtained between the present numerical results and experimental results when Re is small. However, for high-Re cases, the mass conservation seems not so good as the low-Re case.

Received 24 December 2008; Revised 9 June 2009; Accepted 10 June 2009

KEY WORDS: lattice Boltzmann; multiphase flow; bubble flow; moving frame; moving boundary; moving reference; large density ratio

1. INTRODUCTION

Multiphase and multi-component flows occur in many natural and industrial processes. Conventionally, the multiphase and multi-component flows are simulated by solving a set of Navier–Stokes (N-S) equations coupled with an equation to track or capture the interface. Among the approaches,

*Correspondence to: Haibo Huang, Department of Modern Mechanics, University of Science and Technology of China, Hefei 230027, China.
†E-mail: huanghb@ustc.edu.cn

Contract/grant sponsor: National Science Foundation of China (NSFC); contract/grant number: 10802085

volume of fluid (VOF) [1, 2] and level set method [3] are applied extensively. However, it is well known that they may encounter some numerical difficulties in the treatment of topological deformation of interface breaking and coalescing. In addition to that, VOF may also be hard to extend to the 3D case due to the difficulty in interface-reconstruction from the values of volume fraction. For the level set method, a re-initialization procedure is required to keep the distance property when large topological changes occur around the interface. This may violate the mass conservation.

The lattice Boltzmann method (LBM), which is based on mesoscopic kinetic equations, has become a promising numerically robust technique for simulating multiphase fluids [4–9]. It has been successfully applied to study wetting and spreading phenomena [10–12], bubble collision and bubble rising phenomena [6, 7], displacement of immiscible fluids in porous media [5, 13, 14], etc.

There are several popular multiphase models in LBM. The first type is the color-gradient-based LBM proposed by Gunstensen *et al.* [15], which is based on Rothman–Keller lattice gas model [16]. The second type is the Shan–Chen-type model [4], in which the nonlocal interaction is incorporated into the lattice Boltzmann (LB) equation and the nonideal-gas's equation of state is constructed through adding the potential form of the interaction into the ideal-gas's equation of state. The third type is free-energy-based LBM [17]. The fourth type is the model of He *et al.*'s [18], in the model, to eliminate the numerical instability caused by large intermolecular force near the interface, two sets of particle distribution function (PDF) and the concept of the index function are used.

For the aspect of the evolution of interface, the first, second and the fourth models do not explicitly describe the evolution of the interface and the physics of the interface capturing equation is unclear. While in the free-energy-based LBM method, a set of PDF is designed to solve the convection-diffusion equation, i.e. a modified Cahn–Hilliard (C–H) equation, which is an evolution equation for the interface. This equation evolves the order parameter (for example, density difference), which is used to distinguish different phases or components. In this sense, the order parameter is quite similar to the indicator of the traditional volume tracking method such as VOF.

Although LBM has made great progress in multiphase flow modeling, most of the above LBMs are limited to small density ratios less than ten because numerical instability may appear in cases of large density ratio. Inamuro *et al.* [6] and Lee and Lin [19] achieve a high density ratio through improving Swift's free-energy model [17] and model of He *et al.* [18], respectively.

In the model of Inamuro *et al.* [6], the pressure correction is applied to enforce the continuity condition after every collision-streaming step, which is similar to VOF method [1] and level set method [3]. The projection step would reduce the efficiency of the method greatly. A small drawback is that the cut-off value of the order parameter and the surface tension coefficient are not analytically given in the model. It is also found that the model may not be accurate for some incompressible flows although the projection procedure is employed to secure the incompressible condition [9].

Lee and Lin [19] developed an LBM for multiphase flows with large density ratio. It is based on the model of He *et al.* [18], hence it still does not completely recover the C-H equation. Besides, at different steps, the discretization forms are different, which make the implementation quite complex.

Based on free-energy-based LBM [17, 20], the LB model of Zheng *et al.* [9] is able to recover the C-H equation without any additional terms and it is able to keep the Galilean invariance property. This model is also found more efficient than other LB models because it is D2Q5 while not D2Q9 particle velocity model is incorporated to recover the C–H equation.

DOI: 10.1002/fld

In this paper, an LB equation with a D3Q7 velocity model for solving C-H equation [21] is applied to solve the 3D C–H equation. Another LB equation with a set of D3Q19 PDF is used to solve N–S equations. This 3D free-energy-based LB model is applied to study the air bubble rising in viscous fluid so as to test this model's performance on large-density-ratio two-phase flows.

2. MODEL AND THEORY

In this study, a flow with two immiscible fluids or phases has large density ratio is considered. The liquid density and gas density are represented by ρ_l and ρ_g, respectively. The N–S equation and the following C–H equation are used to describe the two-phase flows [22–24]:

$$\partial_t n + \partial_\alpha (n u_\alpha) = 0 \tag{1}$$

$$\partial_t (n u_\alpha) + \partial_\beta (n u_\beta u_\alpha) = -\partial_\alpha (p_{\alpha\beta}) + \rho v \partial_\beta (\partial_\beta u_\alpha + \partial_\alpha u_\beta) + F_\alpha \tag{2}$$

$$\partial_t \phi + \partial_\beta (\phi u_\beta) = \theta_M \partial_\beta (\partial_\beta \mu_\phi) \tag{3}$$

In this paper, subscripts $\alpha, \beta, \ldots$ will be used to represent Cartesian coordinates and ∂_t, ∂_α denote differentiation with respect to t and x_α, respectively. A summation over repeated indices is assumed. In above equations, μ_ϕ is the chemical potential, θ_M is the mobility, $p_{\alpha\beta}$ is the pressure tensor, F_α is the body force in the x_α direction and n, ϕ are defined as [24]:

$$n = \frac{\rho_A + \rho_B}{2}, \quad \phi = \frac{\rho_A - \rho_B}{2}$$

where ρ_A and ρ_B are the density of fluids A and B, respectively. They may be ρ_l or ρ_g, depending on the initial conditions.

2.1. The interface capturing equation

In this section we briefly describe how an LB equation with a set of D3Q7 PDFs is able to recover the interface capturing equation, i.e. the C–H equation. To recover the Equation (3), the following slightly modified LB equation is adopted [25]:

$$g_i(\mathbf{x} + \mathbf{e}_i \delta t, t + \delta t) - g_i(\mathbf{x}, t) = (1 - q)[g_i(\mathbf{x} + \mathbf{e}_i \delta t, t) - g_i(\mathbf{x}, t)] + \frac{1}{\tau_\phi}[g_i^{\mathrm{eq}}(\mathbf{x}, t) - g_i(\mathbf{x}, t)] \tag{4}$$

where τ_ϕ is a dimensionless single relaxation time, q is a constant. If q is set to be one, the above Equation (4) is the conventional LB equation. In the equation, g_i is the set of D3Q7 PDF used here to recover the C–H equation and $\mathbf{e}_i$ is the lattice velocity illustrated as follows:

$$[\mathbf{e}_0, \mathbf{e}_1, \mathbf{e}_2, \mathbf{e}_3, \mathbf{e}_4, \mathbf{e}_5, \mathbf{e}_6] = c \cdot \begin{bmatrix} 0 & 1 & -1 & 0 & 0 & 0 & 0 \\ 0 & 0 & 0 & 1 & -1 & 0 & 0 \\ 0 & 0 & 0 & 0 & 0 & 1 & -1 \end{bmatrix}$$

where $c = \delta x / \delta t$ is the lattice speed, which defined as the ratio of lattice spacing δx and time step δt. In our study, we define one lattice unit δx as 1 $l.u.$ and δt as 1 $t.s.$

DOI: 10.1002/fld

The macroscopic variables are evaluated by

$$\phi=\sum_i g_i \tag{5}$$

Applying Chapman–Enskog expansion and Taylor expansion [20, 26] on Equation (4) and retaining terms to $O(\delta t^2)$, we obtain

$$\begin{aligned}&(\partial_t+qe_{i\beta}\partial_\beta)g_i^{(0)}+\delta t\left[\left(\frac{1}{2}-\tau_\phi\right)\partial_t(\partial_t+qe_{i\beta}\partial_\beta)g_i^{(0)}\right.\\&\quad\left.+\left(\frac{2-q}{2}-\tau_\phi q\right)\partial_t(e_{i\beta}\partial_\beta)g_i^{(0)}+\left(\frac{q}{2}-\tau_{\phi q^2}\right)(e_{i\alpha}\partial_\alpha e_{i\beta}\partial_\beta)g_i^{(0)}\right]+O(\delta t^2)\\&=-\frac{1}{\tau_\phi\delta t}(g_i-g_i^{(0)})\end{aligned} \tag{6}$$

The first and second terms of the above equation in brackets is of higher order and can be neglected [20]. To recover the C–H equation, there are three constraints on the zeroth, first and second moments of the equilibrium distribution function,

$$\sum_i g_i^{(0)}=\phi,\quad \sum_i g_i^{(0)}e_{i\alpha}=\frac{\phi}{q}u_\alpha,\quad \sum_i g_i^{(0)}e_{i\alpha}e_{i\beta}=E_{\alpha\beta} \tag{7}$$

Here it should notice that $\sum_i g_i^{(1)}=0$ can be derived from Equation (5) and the above equation. However, it is assumed that $\sum_i g_i^{(1)}e_{i\alpha}\neq 0$ since $\sum_i g_i e_{i\alpha}=(\phi/q)u_\alpha$ is never used or defined. Summing both sides of Equation (6) over i and using these constraints gives,

$$\partial_t\phi+\partial_\beta(\phi u_\beta)+\delta t\left(\frac{2-q}{2q}-\tau_\phi\right)\partial_t[\partial_\beta(\phi u_\beta)]+\delta t\left(\frac{q}{2}-\tau_\phi q^2\right)\partial_\alpha\partial_\beta(E_{\alpha\beta})+O(\delta t^2)=0 \tag{8}$$

Comparing the above equation with Equation (3), it is found that the following two equations should be satisfied:

$$\frac{2-q}{2q}-\tau_\phi=0 \tag{9}$$

$$-\delta t\left(\frac{q}{2}-\tau_\phi q^2\right)E_{\alpha\beta}=\theta_M\mu_\phi\delta_{\alpha\beta} \tag{10}$$

If we defined the mobility as,

$$\theta_M=-\left(\frac{q}{2}-\tau_\phi q^2\right)\delta t\Gamma \tag{11}$$

Equation (10) would give $E_{\alpha\beta}=\Gamma\mu_\phi\delta_{\alpha\beta}$.

Equation (9) further gives

$$q=\frac{1}{\tau_\phi+0.5} \tag{12}$$

DOI: 10.1002/fld

Because in the above procedure, the fourth-order isotropic lattice tensor is not required as the conventional LBMs, here the D3Q7 model is enough to recover the C–H equation. According to the constraints in Equation (7), the equilibrium distribution functions take the following form:

$$g_i^{(0)} = A_i + B_i\phi + C_i\phi e_{i\alpha}u_\alpha \tag{13}$$

The coefficients can be chosen as

$$B_0 = 1, \quad B_i = 0 (i \neq 0) \tag{14}$$

$$C_i = \frac{1}{2q} \tag{15}$$

$$A_0 = -3\Gamma\mu_\phi, \quad A_i = \tfrac{1}{2}\Gamma\mu_\phi \tag{16}$$

where Γ is used to control the mobility.

2.2. The interface modeling

In this section, we discuss the surface tension force modeling.

In Equation (2), the term $\partial_\alpha(p_{\alpha\beta})$ is related to the surface tension force. This term can be written as a potential term [23, 27] $\partial_\alpha(p_{\alpha\beta}) = -\phi\partial_\alpha\mu_\phi - \partial_\alpha p_0$, where $p_0 = nc_s^2 \cdot\ c_s = c/\sqrt{3}$ is the sound speed. As a result, the momentum equation (i.e., Equation (2)) can be rewritten as

$$\partial_t(nu_\alpha) + \partial_\beta(nu_\beta u_\alpha) = -\partial_\alpha(p_0 + \phi\mu_\phi) + \mu_\phi\partial_\alpha\phi + \rho\nu\partial_\beta(\partial_\beta u_\alpha + \partial_\alpha u_\beta) + F_\alpha \tag{17}$$

The chemical potential μ_ϕ can be derived from the free energy density function. We adopt a free energy function in a closed volume with a mixture of two fluids taking the form [23, 28]

$$F = \int \Psi \,\mathrm{d}V = \int \mathrm{d}V \left[\psi(\phi) + \frac{k}{2}(\partial_\alpha\phi)^2 + \frac{n\ln n}{3}\right] \tag{18}$$

Here, V is a control volume, k is a coefficient, which is related to the surface tension and the thickness of the interface layer. ψ is the bulk free energy density per unit mass for the homogeneous system. The square of gradient term is associated with variations of the density and contributes to the free energy excess of the interfacial region, which defines the surface energy [28]. It is chosen as a double-well form

$$\psi(\phi) = A(\phi^2 - \phi^{*2})^2 \tag{19}$$

where A is an amplitude parameter to control the interaction energy between the two phases; ϕ is the order parameter. This form will contribute to two equilibrium states, ϕ^* and $-\phi^*$. The chemical potential is [23]

$$\mu_\phi = \frac{\partial\Psi}{\partial\phi} - \partial_\alpha\left(\frac{\partial\Psi}{\partial(\partial_\alpha\phi)}\right) = A(4\phi^3 - 4\phi^{*2}\phi) - k\partial_\alpha^2\phi \tag{20}$$

The pressure tensor is [23]

$$p_{\alpha\beta} = p\delta_{\alpha\beta} - k[(\partial_\alpha\phi)^2\delta_{\alpha\beta} - \partial_\alpha\phi\partial_\beta\phi] \tag{21}$$

DOI: 10.1002/fld

where

$$p = A(3\phi^4 - 2\phi^{*2}\phi^2 - \phi^{*4}) - k\phi\partial_\alpha^2\phi + \frac{k}{2}(\partial_\alpha\phi)^2 + \frac{n}{3} \tag{22}$$

It should be noted there are some first and second derivatives in above equations and they can be evaluated through finite difference schemes, i.e.

$$\frac{\partial\phi}{\partial x_\alpha} = \sum_{i=1}^{18} \frac{\omega_i e_{i\alpha} \cdot \phi(\mathbf{x} + e_{i\alpha}\delta t)}{c_s^2 \delta t}$$

$$\partial_\alpha^2\phi = 2 \cdot \sum_{i=1}^{18} \frac{\omega_i[\phi(\mathbf{x} + \mathbf{e}_i\delta t) - \phi(\mathbf{x})]}{c_s^2(\delta t)^2}$$

where ω_i are defined later in Equation (28).

Following the same procedure as References [22, 23], we can obtain the order parameter profile along the normal direction of the interface $\phi = \phi^* \tanh(2\zeta/W)$, where ζ is the coordinate, which is perpendicular to the interface, and W is the thickness of interface layer [23],

$$W = \frac{\sqrt{2k/A}}{\phi^*} \tag{23}$$

For a flat interface, the surface tension coefficient can be evaluated as [28] $\sigma = \int k\ (\partial\phi/\partial\zeta)^2 \mathrm{d}\zeta$. Hence, the surface tension coefficient is

$$\sigma = \frac{4AW}{3}\phi^{*4} \tag{24}$$

where the order parameter is $\phi^* = (\rho_l - \rho_g)/2$. In the simulation, usually the ϕ^* is determined by density ratio and the interface thickness is usually specified larger than 4 lattice unit [9]. The surface tension σ is specified by the parameters Mo, Eo in simulation and then the parameter A is fully decided through Equation (24).

2.3. The continuity and momentum equations

After the above discussion on the surface tension force modeling, we discuss the continuity and momentum equations. To recover the N–S equation, here the second LB equation is employed as

$$f_i(\mathbf{x} + \mathbf{e}_i\delta t, t + \delta t) - f_i(\mathbf{x}, t) = \frac{1}{\tau_n}[f_i^{\mathrm{eq}}(\mathbf{x}, t) - f_i(\mathbf{x}, t)] + S_i \tag{25}$$

where τ_n is a relaxation time parameter, which is different from the parameter τ_ϕ and S_i is a source term added into LBE to mimic the body force term, which appears in the N-S equation.

In the above equation, $\mathbf{e}_i$s are the discrete velocities of the D3Q19 model, which are given as

$$[\mathbf{e}_0, \mathbf{e}_1, \mathbf{e}_2, \mathbf{e}_3, \mathbf{e}_4, \mathbf{e}_5, \mathbf{e}_6, \mathbf{e}_7, \mathbf{e}_8, \mathbf{e}_9, \mathbf{e}_{10}, \mathbf{e}_{11}, \mathbf{e}_{12}, \mathbf{e}_{13}, \mathbf{e}_{14}, \mathbf{e}_{15}\mathbf{e}_{16}, \mathbf{e}_{17}, \mathbf{e}_{18}]$$

$$= c \cdot \begin{bmatrix} 0 & 1 & -1 & 0 & 0 & 0 & 0 & 1 & 1 & -1 & -1 & 1 & -1 & 1 & -1 & 0 & 0 & 0 & 0 \\ 0 & 0 & 0 & 1 & -1 & 0 & 0 & 1 & -1 & 1 & -1 & 0 & 0 & 0 & 0 & 1 & 1 & -1 & -1 \\ 0 & 0 & 0 & 0 & 0 & 1 & -1 & 0 & 0 & 0 & 0 & 1 & 1 & -1 & -1 & 1 & -1 & 1 & -1 \end{bmatrix}$$

DOI: 10.1002/fld

Here the body force term that appears in the above N–S equation is $F_\alpha+\mu_\phi\partial_\alpha\phi$, then the source term can take the following form:

$$S_i=\frac{e_{i\alpha}\omega_i}{c_s^2}(F_\alpha+\mu_\phi\partial_\alpha\phi) \tag{26}$$

To recover the NS equations through Chapman–Enskog expansion, there are several constraints that should be satisfied:

$$\begin{gathered}\sum_i f_i^{(0)}=n,\quad \sum_i f_i^{(0)}e_{i\alpha}=nu_\alpha \\ \sum_i f_i^{(0)}e_{i\alpha}e_{i\beta}=(\phi\mu_\phi+c_s^2n)\delta_{\alpha\beta}+nu_\alpha u_\beta\end{gathered} \tag{27}$$

From these constraints, the equilibrium PDFs are constructed as follows:

$$f_i^{(0)}=\omega_i A_i+\omega_i n\left(\frac{e_{i\alpha}u_\alpha}{c_s^2}+\frac{e_{i\alpha}u_\alpha e_{i\beta}u_\beta}{2c_s^4}-\frac{u_\alpha u_\alpha}{2c_s^2}\right) \tag{28}$$

where the coefficients are chosen as

$$\begin{aligned}A_0&=3n-6(\phi\mu_\phi+c_s^2n)\\ A_i&=3(\phi\mu_\phi+c_s^2n),\quad i=1,2,\ldots 18\end{aligned} \tag{29}$$

In above equations, for the D3Q19 model, $w_i=\frac{1}{3}(i=0)$, $w_i=\frac{1}{18}$, $(i=1,2,\ldots,6)$, $w_i=\frac{1}{36}$, $(i=7,8,\ldots,18)$. n is the density of the fluid, which can be obtained from $n=\sum_i f_i$.

2.4. Moving reference frame

As we know, the computational domain size in the vertical direction may be very large to allow the bubble long-time rising vertically. Applying a moving reference is a good strategy to perform the long-time simulation of a single bubble rising with a limited computational resource. To mimic a moving frame, which is moving with a constant velocity, the inlet and outlet velocity boundaries would be specified for top and bottom horizontal planes, respectively, while moving wall boundary conditions specified for vertical wall boundaries. To handle these boundary conditions, we used the extrapolation method.

The implementation details are explained as follows. Before streaming step is implemented, the PDFs in moving wall boundary or top/bottom boundary are calculated as [29]

$$f_i(\mathbf{x}_\mathrm{b},t)=f_i^{\mathrm{eq}}(\mathbf{x}_\mathrm{b},t)+(1-1/\tau_n)(f_i(\mathbf{x}_\mathrm{f},t)-f_i^{\mathrm{eq}}(\mathbf{x}_\mathrm{f},t)) \tag{30}$$

where $\mathbf{x}_\mathrm{b}$ is the boundary node, $\mathbf{x}_\mathrm{f}$ is the nearby fluid node. $g_i(\mathbf{x}_b,t)$ is also calculated in the similar way. The $f_i^{\mathrm{eq}}(\mathbf{x}_b,t)$ and $g_i^{\mathrm{eq}}(\mathbf{x}_\mathrm{b},t)$ are calculated through Equations (28) and (13), respectively, because the velocity is specified and $\phi(\mathbf{x}_\mathrm{b})$, $n(\mathbf{x}_\mathrm{b})$ are able to be extrapolated from the nearby fluid nodes.

As we know, in LBM usually if $U_{\max}/c_s<0.15$, the compressibility effect is negligible [26]. In a simulation if Reynolds number is known, the parameter τ_n should be chosen using the above incompressible constraint. Parameter study shows that numerical results are not sensitive to the variation of τ_ϕ. τ_ϕ usually can be chosen in the range of $[0.65, 0.9]$ and in our simulations τ_ϕ was set as 0.7.

DOI: 10.1002/fld

3. RESULTS AND DISCUSSIONS

Before numerical verifications, we introduce some commonly used nondimensional parameters in bubble rising studies. These parameters are Eo, Mo and Re. Eo is the $Eotvos$ number, $Eo = gd_e^2\rho_l/\sigma$. Mo is the Morton number defined as $Mo = g\mu^4/(\rho_l\sigma^3)$ and Reynolds number is defined as $Re = \rho_l d_e U_\infty/\mu$. The characteristic length, $d_e = (6V/\pi)^{1/3}$, is the volume-equivalent diameter. V is the bubble volume and U_∞ is based on the observed rising velocity [30]. Because we are interested in the high-density-ratio flow, hereafter in all our simulations, density ratio of liquid and gas is 1000 and viscosity ratio is 100. The parameter Γ in all of our simulations were set as 1000 and the thickness of surface interface was set as 4.0. Although Γ and interface thickness W are chosen independently, the results in terms of rising velocity or bubble shape seem not sensitive to Γ or W. Usually the Γ is suggested to choose as small as possible if the numerical instability does not appear [9].

3.1. Moving-reference-frame verification

In our simulations, a moving frame was introduced to perform the long-time simulation of a single bubble rising. First, we would like to verify this strategy. A bubble rising case with $Eo = 243$, $Mo = 266$ was simulated in both a moving frame and two stationary frames. The main parameters of our simulations are listed in Table I. Case A1 was performed in a moving frame and A2, A3 were performed in stationary frames. The difference between case A2 and A3 is that smaller bubble size ($d_e = 30$) and computational domain are used in case A3. Hereafter, the τ_n listed in the Table means the τ_n applied in liquid area. While in the gas (bubble) area, the relaxation parameter is $\tau_n^b = 10 \times (\tau_n - 0.5) + 0.5$ because the viscosity ratio is 100. The criteria distinguishing gas and liquid is $\phi = 0$.

The velocity of moving frame of A1 is set as $U_m = -0.0075 lu/ts$, which is slightly higher than bubble terminal velocity $U_\infty = 0.00647 lu/ts$, which is calculated from the experimental terminal Reynolds number 7.77 [30]. Actually the velocity of moving frame U_m is usually set as a value around the terminal velocity so as to make the bubble moves only around the middle of the computational domain. In this way, long-time simulation is possible and excessive computational resources would be avoided.

The bubble shapes predicted in stationary and moving frames at different nondimensional times are shown in Figure 1. The nondimensional time is defined as $t^* = vt/d_e^2$, where t is the time step value in a simulation. It is found in cases A1 and A2, the bubble shapes are almost identical. In stationary frames, the discrepancy between the shapes obtained in cases A2 and A3 are negligible. It seems that the bubble represented by 30 lattice units is able to give an accurate result.

A comparison of the velocity profiles of bubble rising in case A1 (moving reference frame) and case A3 (stationary reference frame) is shown in Figure 2. In the figure, bubble rising velocity is normalized by U_∞ calculated from the experimental terminal Reynolds number 7.77 [30].

Table I. Parameters in simulations in stationary and moving reference frames.

Test case	Frame	Domain size	d_e	τ_n	U_m	σ	F_z
A1	Moving	$200 \times 200 \times 260$	40	0.6	-0.0075	0.02655	0.00403
A2	Stationary	$200 \times 200 \times 500$	40	0.6	—	0.02655	0.00403
A3	Stationary	$150 \times 150 \times 400$	30	1.0	—	0.885	0.23895

DOI: 10.1002/fld

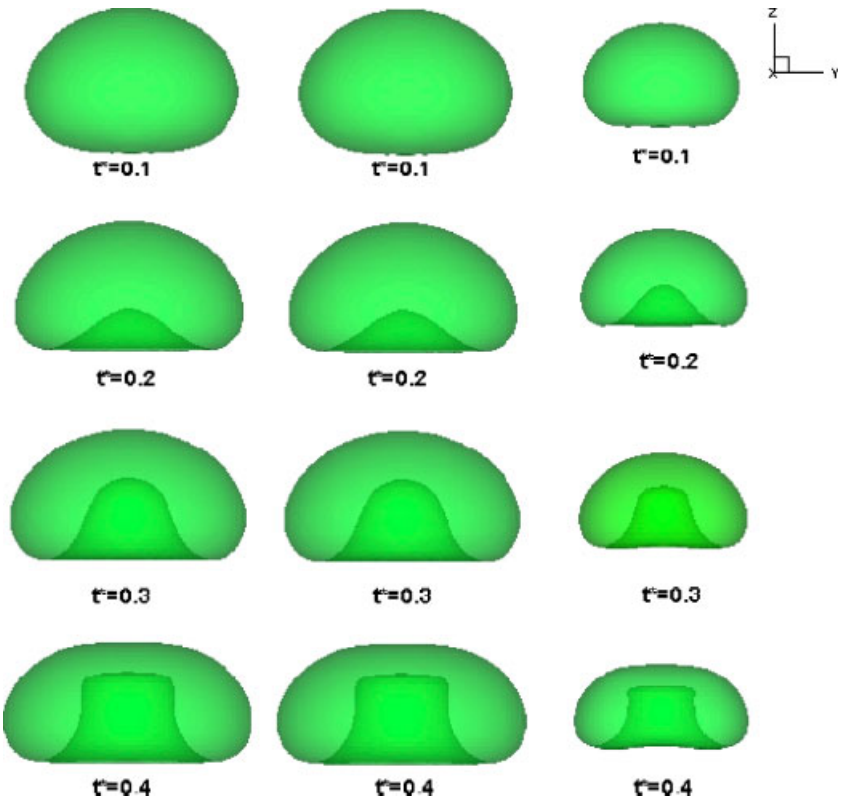

Figure 1. A comparison of the evolution of the predicted bubble shapes in a moving frame (the left column describes case A1) and two stationary frames (the middle column describes the case A2, the right column describes the case A3) under the condition of $Eo = 243$, $Mo = 266$, $\rho_l/\rho_g = 1000$, $\mu_l/\mu_g = 100$.

It should be noted that the velocity of the moving frame itself has been added to the velocity obtained in the moving frame, such that we can make a comparison with the velocity obtained in the stationary frame directly. The bubble rising velocities obtained from the two frames seem to agree well.

The above comparison of bubble shapes and rising velocities in stationary frames and a moving frame verified our strategy of applying moving reference frame. Hereafter we apply this strategy to all of our simulations.

3.2. Model validation with experiments

In this section, to validate our model, we compare our numerical results with the experimental results [30]. As we know, bubble-rising experiments are usually performed in a large tank to eliminate the wall boundary effect. In Bhaga and Weber's experiment [30], the diameter of the tank is about 15 times that of the bubble. However, in numerical simulations, a large computational domain means that excessive computational time and memory are needed to finish the simulation. On the other hand, due to the wall confinement, the computational domain size does have some

DOI: 10.1002/fld

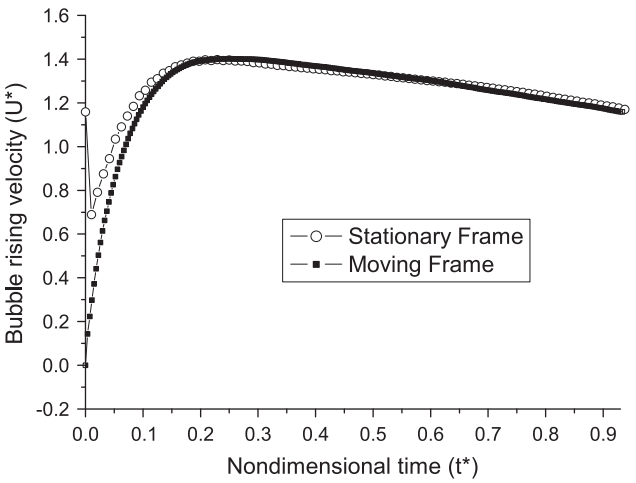

Figure 2. A comparison of the bubble rise velocities predicted in moving and stationary reference frames under the condition of $Eo=243,\ Mo=266,\ \rho_l/\rho_g=1000,\ \mu_l/\mu_g=100$.

effect on the bubble rising velocity and bubble shape [31], a large computational domain is preferred to get accurate results. Hence, we should choose a reasonable domain size to balance these considerations.

To evaluate the effect of the computational domain size on the bubble rising velocity, we simulated two cases with the same parameters $Eo=116$ and $Mo=848$. In the first case, the domain size is $121\times121\times240$ and in the second it is $91\times91\times240$. The initial spherical bubble radius is 30 lattice units in both cases. The terminal bubble velocity should be about 0.00823 lu/ts, which is calculated from Reynolds number measured by Bhaga and Weber [30]. Figure 3 shows the predicted bubble rising velocity of the above two cases. It is found that the terminal bubble velocity in the former case is about $0.00850 lu/ts$ and very close to the value $0.00823 lu/ts$. While bubble terminal velocity predicted by the latter case has a large discrepancy with the experimental value. The terminal bubble shape of the former case is also found more closer to experimental result than the latter case (not shown). Hence, the computational domain size should be at least 4 times the size of the bubble to eliminate the wall effect.

In the following simulations, the computational domain size $L_x\times L_y\times L_z$ is chosen as $L_x=L_y=4d_e$ and $L_z=8d_e$. Bubble's diameter d_e is usually represented by 30 lattice units.

Then six typical cases were further studied to evaluate this model. The nondimensional parameters, measured Reynolds number and the dimensional parameters we used are listed in Table II. The velocities of moving frame in all cases are also listed in the Table. The U_ms are calculated from the terminal Re in experiments [30]. The criteria of choosing dimensional parameter are that σ should not be too high because numerical error may increase or instability may appear. If the interface width is set as 4.0, usually σ should be less than 5.0. In the LBM, after the incompressible constraint is satisfied, the higher τ_n is preferred because it requires less CPU time than a lower τ_n case to reach the same nondimensional time level if the two cases have the same Re number and characteristic length.

DOI: 10.1002/fld

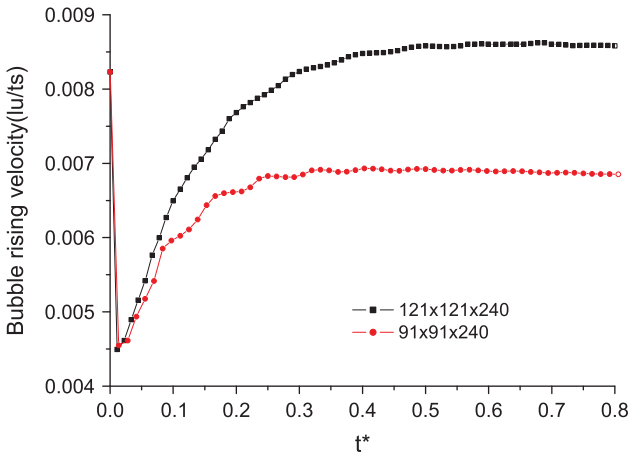

Figure 3. A comparison of the bubble rising velocity in different computational domain sizes.

Table II. Nondimensional and dimensional parameters for three typical test cases.

Test case	Eo	Mo	Re [30]	d_e	τ_n	U_m	F_z	σ
B1	17.7	711	0.232	30	2.0	−0.0039	0.02586	1.3148
B2	32.2	8.2×10^{-4}	55.3	30	0.6	−0.0614	0.26259	7.3393
B3	116	848	2.47	30	1.0	−0.0137	0.04414	0.3425
B4	116	41.1	7.16	30	0.8	−0.0239	0.07218	0.56
B5	116	5.51	13.3	30	0.6	−0.0148	0.0219	0.1699
B6	115	4.63×10^{-3}	94	40	0.55	−0.0392	0.07866	1.094

The terminal bubble shapes of cases B1, B2 and B3 are illustrated in Figure 4. In Figure 4, it is found that these predicted terminal bubble shapes agree well with those observed in experiments [30]. The bubble shapes at time $t^*=0.89$, 0.44, 0.125 for cases B4, B5 and B6, respectively, are also very close to the terminal shape observed in experiments [30]. In case B6, it is found that the bubble deforms and rises in an oscillatory manner in our simulation, which is not consistent with the experimental result.

Figure 5 illustrates the velocities in moving-reference frames as a function of nondimensional time in cases B1–B6. In cases B1, B2 and B3, bubble velocities first increase and then decrease toward a constant value. In these cases, the terminal bubble velocities in their moving frames are all very close to 0, hence the terminal rising velocity in the stationary reference frame and Re would be close to those measured in experiments [30].

Table III shows a comparison of the terminal rise velocities in the stationary reference frame. Our numerical predictions are listed in the fourth column (Re_n). They agree well with the experimental data (i.e., the column 'Re [30]') in cases B1, B2 and B3. It is also noted that the numerically

DOI: 10.1002/fld

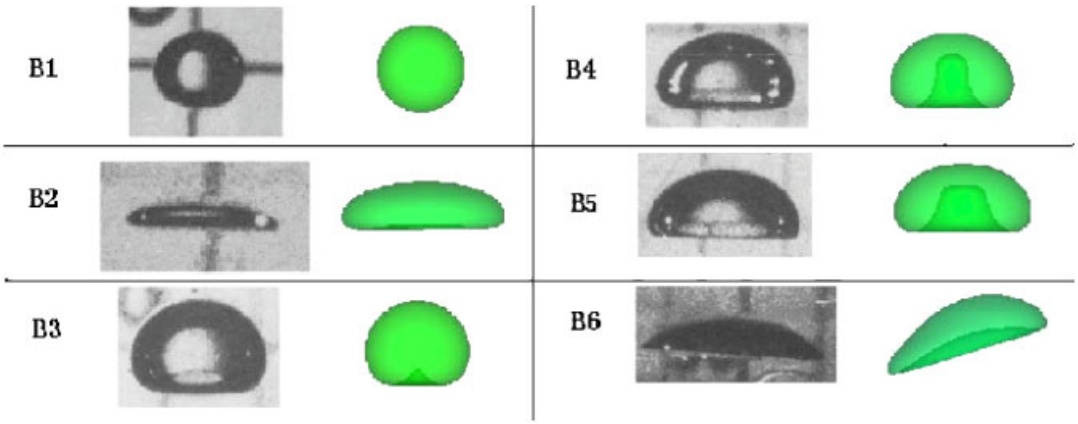

Figure 4. A comparison of the bubble shapes of numerical and experimental results [30]. In each comparison, the left and the right are the experimental and numerical one, respectively. The bubble shapes of cases B1, B2 and B3 are terminal shapes while in cases B4, B5 and B6, the bubble shapes at time $t^* = 0.89$, 0.44, 0.125, respectively, are shown.

predicted Reynolds number is about 20% lower than that observed in experiments in case B1. This deviation is also observed in Reference [31] (the third column), which is obtained by a front tracking method. The wall confinement effect is attributed to the deviation because the effect may be relatively high for very-low-Re cases [31]. For the B2 case, computed Re_n is 16.9% higher than that of the experiment. That may be due to the wall confinement effect which becomes more prominent since the bubble's diameter becomes large and closer to the walls. If a larger computational domain is adopted, this discrepancy may become smaller. In cases B4 and B5, the rising velocity seems not to be decreasing to a constant hence the terminal velocity is unable to determine (refer to Figure 5). In case B6, the bubble volume decreases very quickly and the terminal rising velocity is unable to determine.

3.3. Mass-conservation issue of the method

The mass conservation is an important issue in multiphase flow simulation. As we know, the VOF methods are able to conserve mass exactly as they usually involve a step of interface reconstruction. For the level set or present phase-field method, there are no interface-reconstruction steps and the mass conservation may not so be good. Figure 5 illustrates how the bubble volumes (represent by lattice nodes) change with time in cases B1–B6.

As we can see in Figure 5, the initial lattice nodes inside a bubble of diameter $30lu$ is about $4\pi/3 \times (D/2)^3 = 14\,137$. The bubble volumes seem always decreasing with time. It means that the mass is not conserved exactly in these cases. The mass-conservation in cases B1, B3, B4 and B5 seems much better than in the cases B2 and B6, which has higher Re.

Here we can see that in terms of mass conservation, this method's performance may be similar to that of the level set method, in which mass cannot be conserved exactly. Nevertheless, the model can give a decent result with a minimum effort (without reconstruction) compared with the VOF method.

DOI: 10.1002/fld

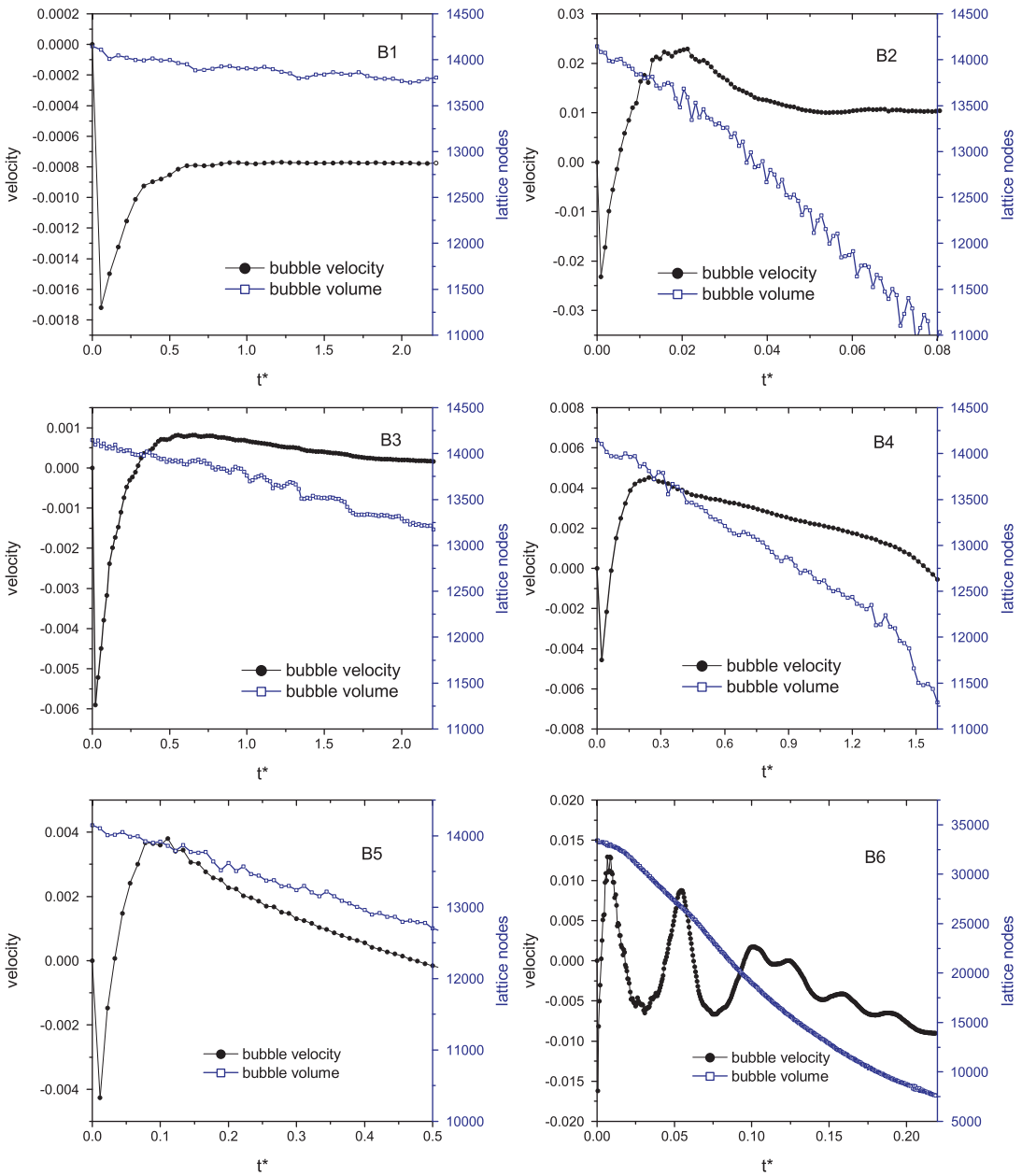

Figure 5. The bubble rising velocity and bubble volume as function of nondimensional time. They describe the bubble rising velocity and bubble volume change for cases B1 to B6, respectively. The velocities are all referred as those in moving-reference frames (refer to Table II for the U_m).

DOI: 10.1002/fld

Table III. Comparison of numerical results and experimental results.

Test case	Re [30]	Re_h [31]	Re_n	$(Re_n - Re)/Re$
B1	0.232	0.182	0.1856	−20%
B2	55.3	54.798	64.62	+16.90%
B3	2.47	—	2.499	+1.17%
B4	7.16	—	—	— %
B5	13.3	—	—	— %
B6	94	89.64	—	—%

4. CONCLUSIONS

In this paper, 3D N–S equation and C–H equation are solved by a free-energy-based multiphase LB model. A method used to handle the inlet/outlet and moving-wall boundary conditions are introduced and these boundary conditions are simple and easy for implementation.

It is demonstrated that the present approach is able to simulate multiphase flows with density ratio as large as 1000 and different viscosities when *Re* is small. In terms of bubble terminal velocity and shape, good agreement was obtained between the present numerical results and experimental results when *Re* is small. The mass conservation of this 3D model was also investigated and it is found for small *Re* cases, the mass conservation is good and acceptable. Our future work is to provide with this method better mass conservation to simulate high-*Re* multiphase flows.

ACKNOWLEDGEMENTS

Huang was supported by the National Science Foundation of China (NSFC) under Grant No.10802085.

REFERENCES

1. Hirt CW, Nichols BD. Volume of fluid (VOF) methods for the dynamics of free boundaries. *Journal of Computational Physics* 1981; **39**:201–225.
2. Rudman M. A volume-tracking method for incompressible multifluid flows with large density variations. *International Journal for Numerical Methods in Fluids* 1998; **28**:357–378.
3. Sussman M, Fatemi E, Smereka P, Osher S. An improved level set method for incompressible two-phase flows. *Computers and Fluids* 1998; **27**:663–680.
4. Shan X, Chen H. Lattice Boltzmann model for simulating flows with multiple phases and components. *Physical Review E* 1993; **47**(3):1815–1819.
5. Martys NS, Chen HD. Simulation of multicomponent fluids in complex three-dimensional geometries by the lattice Boltzmann method. *Physical Review E* 1996; **53**(1):743–750.
6. Inamuro T, Ogata T, Tajima S, Konishi N. A lattice Boltzmann method for incompressible two-phase flows with large density differences. *Journal of Computational Physics* 2004; **198**(2):628–644.
7. Sankaranarayanan K, Shan X, Kevrekidis IG, Sundaresan S. Analysis of drag and virtual mass forces in bubbly suspensions using an implicit formulation of the lattice Boltzmann method. *Journal of Fluid Mechanics* 2002; **452**:61–96.
8. Permnath KN, Abraham J. Lattice Boltzmann simulations of drop-drop interactions in two-phase flows. *International Journal of Modern Physics C* 2005; **16**(1):25–44.
9. Zheng HW, Shu C, Chew YT. A lattice Boltzmann model for multiphase flows with large density ratio. *Journal of Computational Physics* 2006; **218**:353–371.
10. Kang QJ, Zhang DX, Chen SY. Displacement of a two-dimensional immiscible droplet in a channel. *Physics of Fluids* 2002; **14**(9):3203–3214.

DOI: 10.1002/fld

11. Huang HB, Thorne DT, Schaap MG, Sukop M. Proposed approximation for contact angles in Shan-and-Chen-type multicomponent multiphase lattice Boltzmann models. *Physical Review E* 2007; **76**:066701.
12. Raiskinmaki P, Koponen A, Merikoski J, Timonen J. Spreading dynamics of three-dimensional droplets by the lattice Boltzmann method. *Computational Materials Science* 2000; **18**:7–12.
13. Li H, Pan C, Miller CT. Pore-scale investigation of viscous coupling effects for two-phase flow in porous media. *Physical Review E* 2005; **72**:026705.
14. Sukop M, Huang HB, Lin CL, Deo MD, Oh K, Miller JD. Distribution of multiphase fluids in porous media: comparison between lattice Boltzmann modeling and micro-x-ray tomography. *Physical Review E* 2008; **77**:026710.
15. Gunstensen AK, Rothman DH, Zaleski S, Zanetti G. Lattice Boltzmann model of immiscible fluids. *Physical Review A* 1991; **43**(8):4320–4327.
16. Rothman DH, Keller JM. Immiscible cellular-automaton fluids. *Journal of Statistical Physics* 1988; **52**(3/4):1119–1127.
17. Swift MR, Osborn WR, Yeomans JM. Lattice Boltzmann simulation of nonideal fluids. *Physical Review Letters* 1995; **75**(5):830–833.
18. He XY, Chen SY, Zhang RY. A lattice Boltzmann scheme for incompressible multiphase flow and its application in simulation of Rayleigh–Taylor instability. *Journal of Computational Physics* 1999; **152**(2):642–663.
19. Lee T, Lin CL. A stable discretization of the lattice Boltzmann equation for simulation of incompressible two-phase flows at high density ratio. *Journal of Computational Physics* 2005; **206**:16–47.
20. Swift MR, Orlandini E, Osborn WR, Yeomans JM. Lattice Boltzmann simulations of liquid–gas and binary fluid systems. *Physical Review E* 1996; **54**(5):5041–5052.
21. Zheng HW, Shu C, Chew YT, Sun JH. Three-dimensional lattice Boltzmann interface capturing method for incompressible flows. *International Journal for Numerical Methods in Fluids* 2008; **56**:1653–1671.
22. Jacqmin D. Calculation of two-phase Navier–Stokes flows using phase-field modeling. *Journal of Computational Physics* 1999; **155**:96–127.
23. Kendon VM, Cates ME, Pagonabarraga I, Desplat J-C, Bladon P. Inertial effects in three-dimensional spinodal decomposition of a symmetric binary fluid mixture: a lattice Boltzmann study. *Journal of Fluid Mechanics* 2001; **440**:147–203.
24. Takada N, Misawa M, Tomiyama A, Hosokawa S. Simulation of bubble motion under gravity by lattice Boltzmann method. *Journal of Nuclear Science and Technology* 2001; **38**(5):330–341.
25. Lamura A, Succi S. A lattice Boltzmann for disordered fluids. *International Journal of Modern Physics B* 2003; **17**:145–148.
26. He X, Luo LS. Lattice Boltzmann model for the incompressible Navier–Stokes equation. *Journal of Statistical Physics* 1997; **88**:927–943.
27. Jamet D, Torres D, Brackbill JU. On the theory and computation of surface tension: the elimination of parasitic currents through energy conservation in the second-gradient method. *Journal of Computational Physics* 2002; **182**:262–276.
28. Rowlinson JS, Widom B. *Molecular Theory of Capillarity*. Clarendon: Oxford, 1989.
29. Guo ZL, Zheng CG, Shi BC. Non-equilibrium extrapolation method for velocity and pressure boundary conditions in the lattice Boltzmann method. *Chinese Physics* 2002; **11**:366–374.
30. Bhaga D, Weber ME. Bubbles in viscous liquids: shapes, wakes and velocities. *Journal of Fluid Mechanics* 1981; **105**:1–85.
31. Hua J, Stene JF, Lin P. Numerical simulation of 3D bubbles rising in viscous liquids using a front tracking method. *Journal of Computational Physics* 2008; **227**:3358–3382.

DOI: 10.1002/fld